Gold@Prussian blue analogue core–shell nanoheterostructures: their optical and magnetic properties

Guillaume Maurin-Pasturel, Ekaterina Mamontova, Maria A Palacios, Jérôme Long, Joachim Allouche, Jean-Charles Dupin, Yannick Guari, Joulia Larionova

Gold@Prussian blue analogues core-shell nanoheterostructures: their optical and magnetic properties

Guillaume Maurin-Pasturel,[a] Ekaterina Mamontova,[a] Maria A. Palacios,[a] Jérôme Long,*[a] Joachim Allouche,[b] Jean-Charles Dupin,[b] Yannick Guari[a] and Joulia Larionova*[a]

Au@Prussian-Blue Analogues (PBA) shell nanoheterostructures are multifunctional nano-objects combining optical properties (Surface Plasmon Resonance) of the Au core and magnetic properties of the PBA shell. We report in this article a series of new Au core@PBA shell nano-objects with different PBA shells: Au@K/Co/[Fe^{II}(CN)$_6$] (2) and Au@K/Ni/[Cr^{III}(CN)$_6$]:[Fe^{II}(CN)$_6$] (3) single PBA shell, as well as Au@K/Ni/[Fe^{II}(CN)$_6$]@K/Ni/[Fe^{III}(CN)$_6$] (4) double PBA shell and Au@K/Ni/[Fe^{II}(CN)$_6$]@K/Ni/[Fe^{III}(CN)$_6$]@K/Ni/[Cr^{III}(CN)$_6$] (5) triple PBA shell systems. The position and intensity of the Au SPR band, as well as the magnetic behaviour of the nanoheterostructures are strongly affected by the shell composition and its thickness.

Introduction

The design and study of coordination networks, such as Metal-Organic Frameworks (MOFs) or Prussian Blue Analogues (PBAs), continue to attract a huge scientific interest due to their tuneable structures, physical and chemical properties and a large range of potential applications, including gas storage and separation, catalysis, sensors or information storage.[1-5] These systems take advantages from the molecular chemistry approach, which allows to design, by using soft synthetic routes, the molecule-based materials with a great flexibility in their structural organization and the ability to tune their physical properties considering targeted applications. In addition, the control of their size and morphology at the nanoscale permits not only to investigate the impact of the size-reduction effect on physical and chemical properties, but also opens new perspectives for technological applications.

The coordination networks represent also a versatile platform to design multifunctional nanosystems, where several physical properties may be simply combined in the same materials or give birth to new or improved features through a synergic effect.[6] One of the promising strategies to achieve such multifunctionality consists in combining several coordination networks of different chemical composition into core@shell heterostructures. Such approach has been used in the last decade for instance on micron-scaled MOFs giving heterogeneous core@shell MOFs[7-11] or "MOFs-on-MOFs" crystals[12-13] exhibiting optimized porosity, enhanced storage capacity and multifunctionality.[14-18] By using the same approach, core@shell PBA@PBA' nanoparticles have also been designed[19] and reveal different interface-dependent features including an increase in the magnetic coercivity reported for the association of a soft magnetic PBA core with a hard PBA' magnetic shell,[20] an improved photomagnetic effect evidenced in heterostructures made of a photoactive core and a ferromagnetic shell,[21-23,24-25] and an improved rate capability and cyclability for Na$^+$/Li$^+$ ion batteries.[26-27] Such synthetic strategy has recently been extended to other heterostructures made of a Fe(II)- based Hofmann-like network with a spin crossover associated with a ferromagnetic NiCr-PBA to create heterostructurated thin films[28] or nanoparticles.[29]

Another approach to design original multifunctional materials consists in combining coordination networks with inorganic materials of completely different nature. Among the major breakthroughs in the field, most of studies concern the formation of metal or metal oxide nanoparticles embedded in various MOFs using either, post-synthetic incorporation methods or growth of a MOF shell at the surface of metal,[30] metal oxide (Fe$_3$O$_4$),[31] quantum dots[32] or rare-earth nanoparticles.[33] More particularly, the association of gold nanoparticles with various MOFs, such as Zn$_4$O(BDC)$_3$ (BDC=1,4-benzenedicarboxylate),[34a] MIL-100(Fe),[35] ZIF-8 (Zn^{2+} based imidazolate framework)[30] or Cu$_2$(pzdc)$_2$(pyz)[34b] has been reported essentially for their enhanced catalytic features. However, examples of heterostructures with a Au core and a PBA shell are rather scarce despite their potential interest to associate magnetic properties relative to PBA with plasmonic structures of the gold. In this sense, several studies reported on the electrochemical syntheses of hybrid materials containing gold and PBA films,[36-40] or one-pot procedures to combine the gold nanoparticles with PBA.[41,42] However, in these cases there is no clear formation of individual core@shell nanoheterostructures, where a single inorganic nanoparticle is coated with a well-defined shell of a coordination polymer. Therefore, design of such nano-objects represents a synthetic challenge. We have recently reported an original strategy based on a coordination chemistry approach to design Au core@PBA shell heterostructures, Au@K/Ni/[Fe^{II}(CN)$_6$] and Au@K/Ni/[Fe^{II}(CN)$_6$]@K/Ni/[Cr^{III}(CN)$_6$], where the core size and the shell thickness may be thoroughly controlled.[43-44] Remarkably, the shell thickness and composition directly influence the position and intensity of the plasmonic band. On the other hand, the particular architecture of these intricate heterostructures induces a peculiar magnetic behaviour different from single PBA nanoparticles.[44] Encouraged by these results, we pursuit our effort in the investigation and understanding of Au core@PBA shell heterostructures and extend our system to other PBA shells.

In this article, we first investigate by using XPS spectroscopy the gold/PBA interface for Au@K/Ni/[Fe^{II}(CN)$_6$] system with thin and thick PBA shells and identify the species located at the gold surface. Secondly, we show for the first time the possibility to design original systems containing a Au core combined with a single K/Co/[Fe^{II}(CN)$_6$] or a mixed K/Ni/[Cr^{III}(CN)$_6$]:[Fe^{II}(CN)$_6$]] shells. In the latter case, the original nano-objects showing a short-range magnetic transition present a direct contact between the magnetic PBA shell and the plasmonic gold core. Thirdly, the possibility to growth PBA shells on the

surface of other PBA opens the access to Au core multishell systems in which the optical and magnetic properties may be tuned. We demonstrate here that an accurate tuning (coercitivity and critical temperature) of the magnetic properties can be achieved by designing $Au@K/Ni/[Fe^{II}(CN)_6]@K/Ni/[Fe^{III}(CN)_6]$ with double and $Au@K/Ni/[Fe^{II}(CN)_6]@K/Ni/[Fe^{III}(CN)_6]@K/Ni/[Cr^{III}(CN)_6]$ triple PBA shells. While the former system takes advantage of the magnetic anisotropy of the $K/Ni/[Fe^{III}(CN)_6]$ analogue, the latter shows a coupling between the soft $K/Ni/[Cr^{III}(CN)_6]$ external and the hard $K/Ni/[Fe^{III}(CN)_6]$ internal shells.

Experimental

Synthetic procedures

Materials. All chemical reagents were purchased and used without further purification: potassium ferricyanide (Acros Organics, 99%), Gold(I) potassium cyanide (Alfa Aesar), Potassium hexacyanochromate(III) (Aldrich), Nickel(II) chloride hexahydrate (Chimica, 99%), Potassium borohydride (Acros Organics, 98%), Cobalt (II) chloride hexahydrate (Sigma-Aldrich, 98%), ultra-pure water.

Synthesis of the Au nanoparticles. In a typical experiment, KBH_4 (0.63 mmol) was added to 100 mL of an aqueous solution of $K[Au(CN)_2]$ (4.8×10^{-2} mmol) under vigorous stirring at 25°C. The colourless solution rapidly turned red, indicating the formation of Au nanoparticles. After 20 min, they were used immediately in the next step.

Synthesis of $Au@K/Ni/[Fe^{II}(CN)_6]$ core@shell nanoparticles (1a and 1b):

The $Au@K/Ni/[Fe^{II}(CN)_6]$ core@shell nanoparticles were synthesized by the two-step approach as it has been described in our earlier publications.[43-44] Briefly, aqueous solutions of $K_3[Fe(CN)_6]$ (5.65 mM) and $NiCl_2 \cdot 6H_2O$ (5.0 mM) were simultaneously added with a fixed addition rate at 2 mL.h^{-1} to the gold nanoparticles' solution obtained in the previous step under vigorous stirring at 25 °C. The shell thickness is controlled by the volume of the added solution of precursors. The smallest $Au@K/Ni/[Fe^{II}(CN)_6]$ core@shell nanoparticles **1a** were obtained using 2 mL of each precursors' solutions ($K_3[Fe(CN)_6]$ (5.65 mM) and $NiCl_2 \cdot 6H_2O$ (5.0 mM)). The largest $Au@K/Ni/[Fe^{II}(CN)_6]$ core@shell nanoparticles **1b** were obtained using 10 mL of each solutions. After addition, the mixture was vigorously stirred for one hour and then centrifuged at 20000 rpm during 10 min. The obtained purple powdered nanoparticles were washed successively with water and ethanol and dried under vacuum. In the case of **1a,** the pH of the solution was decreased to 4 before centrifugation (5 minutes instead of 10). The supernatant was removed and the nanoparticles were dispersed in water and re-filled until 100 ml for the next step.

Purple powder. IR (KBr): ν_{CN}= 2098 cm^{-1} ($\nu(Fe^{II}$-CN-Ni^{II})) for **1a** and **1b**.

EDS: 12.1/ 17.4/ 11.8/ 58.7 = K/Ni/Fe/Au for **1a**. Formula found: $Au_{3.4}@K_{0.7}Ni[Fe^{II}(CN)_6]_{0.7}$.

Elemental anal. Found (wt %): Au, 41.3 ; K, 9.11 ; Ni, 11.4 ; Fe, 8.67; C, 11.2; N, 13.1 **1b**. Formula found: $Au_{3.6}@K_{0.8}Ni[Fe^{II}(CN)_6]_{0.8}$.

Synthesis of $Au@K/Co/[Fe^{II}(CN)_6]$ core@shell nanoparticles (2):

10 mL of an aqueous solution of $CoCl_2 \cdot 6H_2O$ (5.0 mM) was added (2mL.h^{-1}) to the gold nanoparticles' solution under vigorous stirring at 25°C. After a delay of 30 min., 10 mL of an aqueous solution of $K_3[Fe(CN)_6]$ (5.65 mM) was added to the mixture with the same rate (2ml.h^{-1}) under stirring at 25°C. After completion of the addition, the mixture was vigorously stirred for one hour. The obtained nanoparticles were centrifuged at 20000 rpm during 10 min. The supernatant was removed and the nanoparticles **2** were washed with water and ethanol and then dried under vacuum.

Cobalt blue powder. IR (KBr): ν_{CN}= 2081 cm^{-1} (Fe^{II}-CN-Co^{II}). EDS: 38.7/22.7/20.4/18.2 = K/Co/Fe/Au for **2**. Formula found: $Au_{0.8}@K_{1.7}Co[Fe^{II}(CN)_6]_{0.9}$.

Synthesis of $Au@K/Ni/[Cr^{III}(CN)_6]:[Fe^{II}(CN)_6]$ core@shell nanoparticles (3):

In a typical experiment, 4 mL of an aqueous solution mixture of $K_3[Cr(CN)_6]$ (4.52 mM) and ($K_3[Fe(CN)_6]$ (1.13 mM) giving a total hexacyanometallate concentration of 5.65 mM and 4 mL of an aqueous solution of $NiCl_2 \cdot 6H_2O$ (5.0 mM) were simultaneously added with a fixed addition rate at 2 mL.h^{-1} to the gold nanoparticles' solution under vigorous stirring at 25 °C. After addition, the mixture was stirred for one hour and then centrifuged at 20000 rpm during 10 min. The supernatant was removed and the obtained nanoparticles were washed successively with water and ethanol and dried under vacuum.

Dark violet powder. IR (KBr): ν_{CN}= 2096 cm^{-1} (Fe^{II}-CN-Ni^{II}), ν_{CN}= 2173 cm^{-1} (Cr^{III}-CN-Ni^{II}, Fe^{III}-CN-Ni^{II}). EDS: 20.4/34.0/4.7/11.0/29.9 = K/Ni/Cr/Fe/Au for **3**. Formula found: $Au_{0.9}@K_{0.6}Ni[Cr^{III}(CN)_6]_{0.1}[Fe^{II}(CN)_6]_{0.3}$.

Synthesis of $Au@K/Ni/[Fe^{II}(CN)_6]@K/Ni/[Fe^{III}(CN)_6]$ core@shell@shell nanoparticles (4):

Two aqueous solutions of $K_3[Fe(CN)_6]$ (5.65 mM) and of $NiCl_2 \cdot 6H_2O$ (5.0 mM) were simultaneously added with a fixed addition rate at 2 mL.h^{-1} to an aqueous solution of $Au@K/Ni/[Fe^{II}(CN)_6]$ nanoparticles under vigorous stirring at 25 °C. 10 mL of each precursors' solutions were added to an aqueous solution of **1b** (10 mg of dried nanoparticles dispersed in 50 mL of ultrapure water). After addition, the mixture was vigorously stirred for one hour and then centrifuged at 20000 rpm during 10 min. The obtained mauve powdered nanoparticles were washed successively with water and ethanol and dried under vacuum.

Mauve powder. IR (KBr): ν_{CN}= 2165cm^{-1} (Fe^{III}-CN-Ni^{II}), ν_{CN}= 2094 cm^{-1} (Fe^{II}-CN-Ni^{II}). Elem. anal. found (wt %): Au, 7.3; K, 4.1; Ni, 17.6; Fe, 12.7; C, 15.9; N, 17.1; H, 2.5 for **4**.

Synthesis of $Au@K/Ni/[Fe^{II}(CN)_6]@K/Ni/[Fe^{III}(CN)_6]@K/Ni/[Cr^{III}(CN)_6]$ core@shell@shell@shell nanoparticles (5):

In a typical experiment, 4 mL of an aqueous solution of $K_3[Fe(CN)_6]$ (5.65 mM) and 4 mL of an aqueous solution of $NiCl_2 \cdot 6H_2O$ (5.0 mM) were simultaneously added with a fixed addition rate at 2 mL.h^{-1} to an aqueous solution of **1a** under

vigorous stirring at 25 °C. After addition, the mixture was vigorously stirred for one hour and then centrifuged at 20000 rpm during 10 min. The supernatant was removed and the nanoparticles were dispersed in 100 ml for the next step. Then, 4 mL of an aqueous solution of $K_3[Cr(CN)_6]$ (5.65 mM) and 4 mL of an aqueous solution of $NiCl_2 \cdot 6H_2O$ (5.0 mM) were simultaneously added with a fixed addition rate at 2 mL.h^{-1} to this obtained solution under vigorous stirring at 25 °C. The obtained nanoparticles **5** were washed successively with water and ethanol and dried under vacuum.

Dark violet powder. IR (KBr): v_{CN}= 2097 cm^{-1} (Fe^{II}-CN-Ni^{II}), v_{CN}= 2171 cm^{-1} (Cr^{III}-CN-Ni^{II}, Fe^{III}-CN-Ni^{II}) for **5**. EDS: 15.3/18.0/18.8/9.1/38.6 (K/Cr/Fe/Ni/Au).

Characterization methods

Infrared spectra were recorded as KBr disks on a Nicolet Model 510P spectrophotometer. UV-Vis spectra were collected on a SPECOORD 210 UV-VIS spectrometer. Transmission Electron Microscopy (TEM) observations were carried out at 100 kV (JEOL 1200 EXII). Samples for TEM measurements were deposited from solutions on copper grids. The size distribution histograms were determined using enlarged TEM micrographs taken at magnification of 100K on a statistical sample of *ca.* 300 NPs. HRTEM measurements were performed on a JEOL 2200FS. SEM/EDX microscopy was performed on a FEI Quanta FEG 200 instrument. The powders were deposited on an adhesive carbon film and analyzed under high vacuum. The quantification of the heavy elements was carried out with the INCA software, with a dwell time of 3 µs. In the case of multishell systems, it was not possible to provide an exact formula of the heterostructures due to the presence of identical elements in the different shells.

The XPS measurements were performed on a Thermo K-alpha spectrometer with a hemispherical analyzer and a microfocused (400 µm diameter microspot) monochromatic radiation (Al Kα, 1486.6 eV) operating at 72 W under a residual pressure of 1.10−9 mbar. The pass energy was set to 20 eV. Charge effects, mainly important for hybrid samples, were compensated by the use of a dual beam charge neutralization system (low energy electrons and Ar$^+$ ions), which had the unique ability to provide consistent charge compensation. All spectra were energy-calibrated by using the hydrocarbon peak at a binding energy of 285.0 eV. Spectra were mathematically fitted with Casa XPS software© using a least squares algorithm and a nonlinear Shirley-type background. The fitting peaks of the experimental curves were defined by a combination of Gaussian (70%) and Lorentzian (30%) distributions. Quantification was performed on the basis of Scofield's relative sensitivity factors.

The magnetic properties of nanoheterostructures were studied using a SQUID-MPMS magnetometer working in the temperature range 1.8 – 350 K up to 7 T by using static (direct current (dc)) and dynamic (alternating current (ac)) modes. The data were corrected for the sample holder. The ac magnetic susceptibility measurements were carried out in the presence of a 3 Oe oscillating field in zero or applied external dc field.

Results and discussion

Design and investigation of Au core@PBA single shell systems.

Investigation of the interface in Au@K/Ni/[Fe^{II}(CN)$_6$] core@shell nanoheterostructures 1a and 1b

Au@K/Ni/[Fe^{II}(CN)$_6$] heterostructures **1a** and **1b** with different shell thickness were obtained as previously reported by using the two-step approach consisting in the reduction of the dicyanoaurate precursor [Au(CN)$_2$]$^-$ by potassium borohydride, followed by the time-controlled growth of the cyano-bridged coordination polymer shell at the surface of these gold nanoparticles.[43-44] The reduction of dicyanoaurate at 25 °C rapidly leads to a ruby colour characteristic of the gold nanoparticles formation.[45] Then the PBA shell growth is carried out by simultaneously adding the respective molecular precursors, K$_3$[Fe^{III}(CN)$_6$] and Ni^{II}Cl$_2 \cdot$6H$_2$O, with a controlled addition rate in order to regulate the PBA layer growth at the gold surface without side-nucleation processes. The shell thickness can be modulated by simply varying the amount of these added precursors.

The Infra-red spectra (IR) for **1a** and **1b** (Fig. S1, Electronic Supporting Information (ESI)), Zetametry measurements (ESI), elemental and Energy Dispersive Spectroscopy (EDS) analyses (Table 1), powder X-Ray Diffraction (PXRD) patterns for **1b** (Fig. S2), as well as Transmission Electronic Microscopy (TEM) analyses (Fig. 1a, b, Table 1) confirm their structural and morphological characteristics. Note that the reduction of initially used [Fe^{III}(CN)$_6$]$^{3-}$ moiety to [Fe^{II}(CN)$_6$]$^{4-}$ occurs during the first shell growth due to the presence of the residual borohydride in the reaction medium ([Fe^{III}(CN)$_6$]$^{3-}$/[Fe^{II}(CN)$_6$]$^{4-}$ = + 0.36 V; (B(OH)$_4^-$/BH$_4^-$) = −1.24 V). This fact is clearly observed by IR spectroscopy.[43, 44]

The gold core presents an average size of *ca.* 19 nm with a PBA shell thickness increasing from 6 ± 2 nm for **1a** to 16± 3 nm for **1b** (Fig. 1a, b, Table 1, Fig. S3).

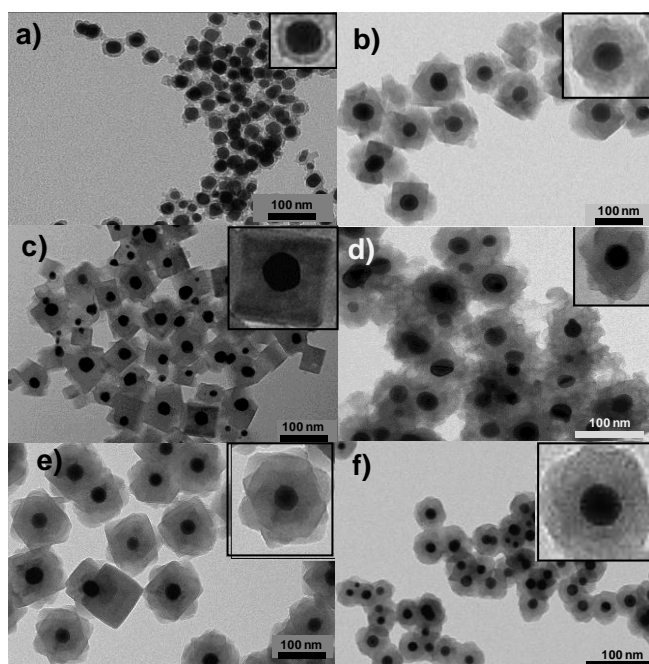To understand the PBA growth mechanism on the surface of the Au nanoparticles and extend the synthetic strategy to other PBA shells, a study of the gold/PBA interface composition within samples **1a** and **1b** was performed using X-Ray Photoelectron Spectroscopy (XPS). This technique is very surface-sensitive due to the collection of electrons emitted from 5 to 10 nm deep in the material. In these conditions, it is possible to monitor an interface when the shell, wrapping a nanoparticle, is thin and/or not dense. The Au4f XPS spectrum of **1a** (Fig. 2) relative to gold is rather complex with the presence of main metallic Au^0 components (Binding Energy (BE) $Au4f_{7/5-5/2}$ = 84.1 - 87.8 eV), Au^I (BE $Au4f_{7/5-5/2}$ = 85.4-89.1 eV) and Au^{III} ones (beyond 86.5 eV for $Au4f_{7/5}$ components). The two latter may be ascribed to the presence of dicyanoaurate(I) and (III) chemical environment, respectively, $[Au(CN)_2]^-$ (Fig. S4) and $[Au(CN)_4]^-$, situated at the interface with the PBA shell.[46] Consequently, it can be supposed that $[Au(CN)_2]^-$ and $[Au(CN)_4]^-$ moieties, localized at the surface of the metallic Au nanoparticles, ensure the coordination with the divalent metal ion (Ni^{2+}). The remaining labile coordination sites on Ni^{2+} can further react with the hexacyanoferrate to allow the growth of a PBA shell.

For the Au4f spectrum of sample **1b**, components ascribed to Au^I are intense and the signal of the metallic Au° is less evident (Au^0/Au^I = 2.35 for **1a** and 0.25 for **1b**) (Fig. 2b). This fact can be explained by the larger shell thickness of **1b**, where the Au^0 nanoparticle core is almost non-visible and the NC-Au^I-CN near-surface functions are more pronounced and well settled all around the gold core. Note that no peaks ascribed for Au^{III} – containing moieties can be observed.
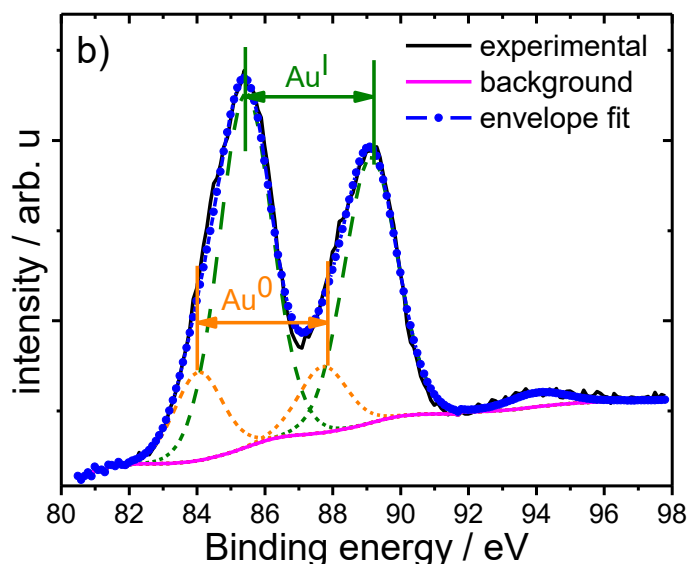

Fig. 2. XPS Au4f core peaks for samples **1a** (a) and **1b** (b). The dashed lines represent the fit components.

The N1s spectrum of sample **1a** (Fig. S5) corroborates these assumptions with a component at 399.0 eV for Au^I-CN^- environment as found in this study for the complex of reference $K[AuCN_2]$ (BE N1s = 398.9eV).[47] At 398.1 eV (Fig. S5), an intense component is observed and can be associated with Fe^{II}-CN^- environment like in the reference complex $K_4[Fe(CN)_6]$. For sample **1b**, only this component (at 398.1 eV) is recorded as the CN^- functions of the PBA shell are in great amount. This shell probably masks the presence of CN^- attached to Au^I. As the PBA shell is thin enough (less than 6 nm), the XPS offers an overview of the PBA/Au core interface with specific local environments of gold and nitrogen.
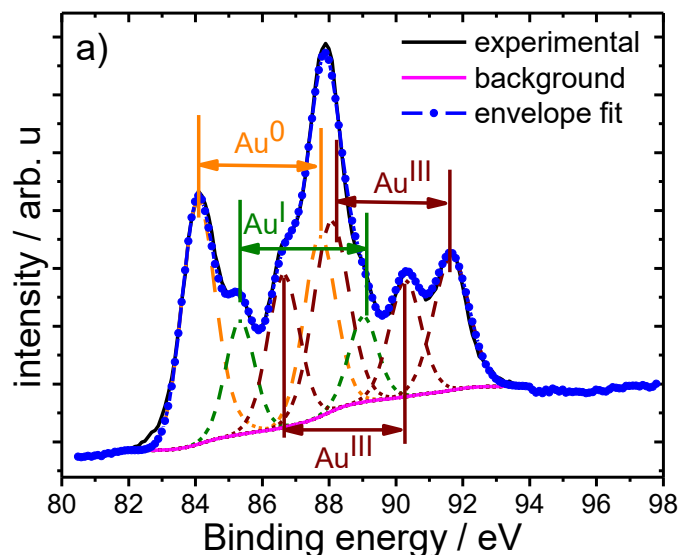
Table 1: Parameters for the core@shell nanoparticles **1-5**.

Label	Composition	Core size (nm)	1st shell thickness (nm)	2nd shell thickness (nm)	3rd shell thickness (nm)	Total shell size (nm)	Total NPs size (nm)
1a	Au@K/Ni/[Fe^{II}(CN)$_6$]	19 ± 5	6 ± 2	-	-	6 ± 2	31 ± 5
1b	Au@K/Ni/[Fe^{II}(CN)$_6$]	19 ± 5	16 ± 3	-	-	16 ± 3	52 ± 9
2	Au@K/Co/[Fe^{II}(CN)$_6$]	20 ± 4	16 ± 4	-	-	16 ± 4	52 ± 7
3	Au@K/Ni/[Cr^{III}(CN)$_6$]:[Fe^{II}(CN)$_6$]	19 ± 3	26 ± 3	-	-	26 ± 3	70 ± 8
4	Au@K/Ni/[Fe^{II}(CN)$_6$]@K/Ni/[Fe^{III}(CN)$_6$]	16 ± 4	18 ± 5	14 ± 3	-	32 ± 8	81± 11
5	Au@K/Ni/[Fe^{II}(CN)$_6$]@K/Ni/[Fe^{III}(CN)$_6$] @K/Ni/[Cr^{III}(CN)$_6$]	19 ± 3	5 ± 4	3 ± 4	5 ± 4	13 ± 4	46 ± 5

Moreover, as expected, for both samples **1a** and **1b**, the presence of Ni2p$_{3/2}$ (BE 856.3eV) and Fe2p$_{3/2}$ (BE 708.4eV) are in accordance with the CN-Ni^{II}-NC-Fe^{II}-CN linkage reported by Kumar *et al.* proving the presence of the PBA shell.[48]

Au@K/Co/[Fe^{II}(CN)$_6$] core@shell nanoheterostructures 2

Each PBA presents a specific kinetic of formation that may depend on the lability/inertness character of the divalent metal ion, as well as the nitrogen basicity of the cyano-ligand belonging to the hexacyanometallate moiety. Furthermore, the strength of the coordination bond between the divalent metal ion and the cyano groups at the surface of the gold nanoparticles may also be relevant to promote the shell growth. For this reason, the working conditions should be adapted for the growth of other PBA shell than K/Ni/[Fe^{II}(CN)$_6$]. By replacing the [Ni(H$_2$O)$_6$]$^{2+}$ complex by [Co(H$_2$O)$_6$]$^{2+}$, with the same experimental conditions, as we used for the synthesis of **1a** and **1b**, only a minor population of core@shell heterostructures was obtained, the main species being isolated K/Co/[Fe(CN)$_6$] and gold nanoparticles (Fig. S6). However, it turns out that delaying the addition time of the hexacyanoferrate moiety by 30 min. with respect to the addition of the [Co(H$_2$O)$_6$]$^{2+}$ complex induces a strong decrease in the population of such isolated nanoparticles with a percentage estimated at 20 %. Such behaviour may be rationalized by the fact that the Co^{2+} ion requires additional time than Ni^{2+} to be strongly coordinated by the surface cyano-groups. Varying the delay time did not lead to a higher population of the targeted heterostructures. Similarly than for **1a** and **1b**, a complete reduction of the hexacyanoferrate moiety is observed by IR spectroscopy (Fig. S7), which shows an asymmetric single peak located at 2081 cm^{-1} attributed to the Fe^{II}-CN-Co^{II} stretching vibrations.[49] A weak peak at 2141 cm^{-1} can be ascribed to a very small proportion of Fe^{II}-CN-Co^{III} pairs. The cell parameter of K/Co/[Fe(CN)$_6$] a_{CoFe} = 10.04 Å obtained from PXRD pattern (Fig. S8) is in agreement with the value of 10.08 Å observed for the bulk K$_2$Co[Fe^{II}(CN)$_6$] (01-075-0038). Scherrer's formula used to estimate the crystalline domains gives a size of 11 nm for the gold core (d$_{111}$ reflection) and *ca.* 26 nm for the K/Co/[Fe^{II}(CN)$_6$] shell (d$_{200}$ reflection) giving a total size of about 64 nm. The crystalline domain size of the PBA is most likely overestimated due to the presence of single PBA nanoparticles (20 %). TEM images confirm the formation of the targeted heterostructures with a gold core size of around 20 nm, while the shell thickness is estimated around 16 nm giving a total size of 52 nm (Fig. 1c, Table 1). Note that the overall morphology for **2** is different from **1a** and **1b** with the formation of a single PBA cubic shell surrounding the gold core. Such fact may be rationalized by differences in the growing kinetic between the PBA shell depending on the transition metal ion nature. This confirms that the original synthetic strategy may be extended to various PBAs by modulating the experimental conditions of the shell growth.

Au@K/Ni/[Cr^{III}(CN)$_6$]:[Fe^{II}(CN)$_6$] core@shell nanoheterostructures 3

The growth of a solid solution of K/Ni/[Cr^{III}(CN)$_6$]:[Fe^{II}(CN)$_6$] shell on the gold nanoparticles' surface was investigated due to the fact that our attempts to directly growth the paramagnetic [Cr^{III}(CN)$_6$]$^{3-}$ shell were unsuccessful. Comparable to the synthesis of **1b**, a mixture of K$_3$[Cr^{III}(CN)$_6$] and K$_3$[Fe^{III}(CN)$_6$] having a total concentration in hexacyanometallate of 5.65 mM was used. IR spectrum for **3** (Fig. S9) exhibits two bands in the cyanide's stretching window, at 2172 and 2095 cm^{-1}, characteristic of Cr^{III}-CN-Ni^{II} and Fe^{II}-CN-Ni^{II} linkages confirming the presence of both cyanometallates in the shell. The PXRD pattern (Fig. S10) clearly shows the presence of the Au core and the hexacyanometallates shells, while due to the close proximity of the peaks for both PBA, it was not possible to clearly distinguish the presence of each of them. This also precludes a relevant Scherrer analysis related to the shell size, while such methodology affords a gold crystalline size of 18 nm.

The initial ratio of precursors [Cr^{III}(CN)$_6$]$^{3-}$/[Fe^{III}(CN)$_6$]$^{3-}$ = 4 gave well defined core@shell nanoparticles, where the Au core is surrounded by the PBA shell, as it can be seen from TEM image (Fig. 1d). As usual, the gold core presents an average size of *ca.* 19 nm with the total PBA shell thickness estimated at *ca.* 26 nm (Table 1). The topochemical distribution by using STEM-HAADF (Fig. S11) clearly confirms the presence of the gold core and the homogeneous distribution of iron and chromium atoms within the PBA shell. Noticeably, the Cr/Fe ratio of 0.42 obtained by EDS is one order of magnitude lower than the introduced ratio, confirming the special affinity of the hexacyanoferrate moiety with the gold nanoparticles.

Design of Au core PBA multishell nanoheterostructures

Au core@PBA shell@PBA shell nanoheterostructures 4

We have previously reported the use of Au@ K/Ni/[Fe^{II}(CN)$_6$] heterostructures as starting materials to subsequently design Au@K/Ni/[Fe^{II}(CN)$_6$]@K/Ni/[Cr^{III}(CN)$_6$] nanoheterostructure by

the growth of one PBA shell on the other.[43-44] In this system, spin-glass behaviour was evidenced due to the peculiar architectures and the spin frustration at interfaces.

We show here that it is possible to extend this strategy to other magnetic PBA analogues, such as for instance $K/Ni/[Fe^{III}(CN)_6]$ exhibiting substantial magnetic coercivity with respect to the isotropic $K/Ni/[Cr^{III}(CN)_6]$ analogue. Risset and Talham have recently demonstrated that small lattice misfits between the seeds and the overlayer is one of the main prerequisites for the formation of regular core@shell architectures by epitaxial growth without island formation.[50] The lattice mismatch between the cell parameters of the first $K/Ni/[Fe^{II}(CN)_6]$ and the second $K/Ni/[Fe^{III}(CN)_6]$ shells is estimated at 1.6 %, which should be considered as satisfactory. After isolation of the pristine $Au@K/Ni/[Fe^{II}(CN)_6]$ heterostructures **1b**, the growth of the second PBA shell can be achieved by slow addition of the molecular precursors, $NiCl_2 \cdot 6H_2O$ and $K_3[Fe^{III}(CN)_6]$. The IR spectra of compound **4** (Fig. S12) shows two peaks at 2098 and 2165 cm^{-1}, which can be ascribed to the Fe^{II}-CN-Ni^{II} and Fe^{III}-CN-Ni^{II} vibrations, respectively. PXRD pattern performed for sample **4** (Fig. S13) does not show the distinct peaks permitting to well distinguish both PBA shells due to the close proximity of the peaks' position for reduced and oxidized PBA forms. We note however the asymmetric shape of the peaks corresponding to the (222) and (400) reflections. The cell parameter is found equal to a_{NiFe} = 10.20 Å, which is close to the value of 10.23 Å found for the bulk $Ni_3[Fe(CN)_6]_2$ (00-046-0906), while the reduced PBA exhibits a cell parameter of 10.08 Å (00-046-0908). Scherrer's formula application gives a size of 16 nm for the gold core (d_{111} reflection) and *ca.* 29 thickness nm for the total shell (d_{200} reflection) giving a total size of about 74 nm. This value is in excellent agreement with the total size of nanoparticles of 81 nm obtained from TEM (Fig. 1e, Fig. S3, Table 1). The latter clearly confirms the growing of the second PBA shell with an increase of the total size of the nanoparticles. The second shell thickness is estimated to *ca.* 14 nm (obtained from the difference between the double and single shell nanoparticles). TEM images reveal a complex morphology of the as-obtained heterostructures consisting in several cubic shells, which have been grown on different facets of the gold core yielding to a flower-like architecture (Fig. 1e).

Au core@PBA shell@PBA shell@PBA shell nanoheterostructures 5

With the aim to design sophisticated magneto-plasmonic systems, it is possible to engineer multiple shell systems. In this sense, we have chosen to combine, the high magnetic ordering temperature of the $K/Ni/[Cr^{III}(CN)_6]$ PBA with the high coercivity of $K/Ni/[Fe^{III}(CN)_6]$ analogue. Such systems can be easily designed by applying the same strategy than for **4**, but starting with the double shell systems $Au@K/Ni/[Fe^{II}(CN)_6]@K/Ni/[Fe^{III}(CN)_6]$ with a very small first shell thickness and growing a third $K/Ni/[Cr^{III}(CN)_6]$ external shell to give $Au@K/Ni/[Fe^{II}(CN)_6]@K/Ni/[Fe^{III}(CN)_6]@K/Ni/[Cr^{III}(CN)_6]$ **5**. The expected lattice misfit between the two PBA analogues is estimated at 2.2 %. The IR spectra of **5** (Fig. S14) shows the presence of two distinct peaks in the cyanide region located at

2097 and 2171 cm^{-1}, ascribed respectively to the reduced pair Fe^{II}-CN-Ni^{II}, and the envelope between the Fe^{III}-CN-Ni^{II} and Cr^{III}-CN-Ni^{II} linkages. TEM analysis shows the presence of flowers-like heterostructures (Fig. 1f). As usual, the gold core size is of *ca.* 19 nm. The shell thicknesses (determined by measuring the total size at each stages of the synthesis) of *ca.* 5, 3 and 5 nm for the first, second and third shells, respectively, are given in Table 1.

Optical Properties

The optical properties of such heterostructures are dominated by the Surface Plasmon Resonance (SPR) band related to the gold nanoparticles.[51-55] The characteristics (position, intensity, broadness) of this band are extremely sensitive to numerous factors including the size and shape of the gold nanoparticles, as well as the electronic and optical properties of the surrounding medium.[56] We have recently reported the influence of both, the shell thickness and composition on the SPR band in $Au@K/Ni/[Fe^{II}(CN)_6]$ and $Au@K/Ni/[Fe^{II}(CN)_6]@K/Ni/[Cr^{III}(CN)_6]$ heterostructures. Upon increasing the shell thickness, a red shift in the maximum absorption wavelength from 520 nm of the pristine Au nanoparticles is observed as the shell thickness increases.[43-44] This fact has been classically explained by the increase in the local refractive index (n = 1.56 for $Fe_4[Fe(CN)_6]_3$ and n = 1.33 for water) around the gold nanoparticles.

The absorption spectra of all obtained systems were measured in aqueous suspensions. The Au core@PBA single shell systems **1a**, **1b** and **2** show a clear red shift from 520 nm to 533, 538 and 540 nm, respectively, and the drop of intensity as the shell thickness increases, which is consistent with previously described systems (Fig. 3).[44] A minor difference for shells in **1b** and **2** having a comparable shell thickness (*c.a.* 16 nm for $K/Ni/[Fe^{II}(CN)_6]$ and $K/Co/[Fe^{II}(CN)_6]$, respectively) (Fig. 3 a, b) may be explained by different refractive indexes of the two PBA. In contrast, sample **3** (26 nm shell) exhibits an important red-shift up to 560 nm. A red-shift effect can also be observed with double and triple shell systems **4** and **5** (Figures 3a and 3b). Additionally, a progressive increase of the widths of the SPR band with the shell thickness can be ascribed to the confinement of the free electrons within the metal core, as previously observed in the case of the gold nanoparticles coated with TiO_2 shell.[57]

Consequently, these results confirm that modulation of the optical properties can be easily achieved by controlling both, the shell thickness and the PBA chemical composition.
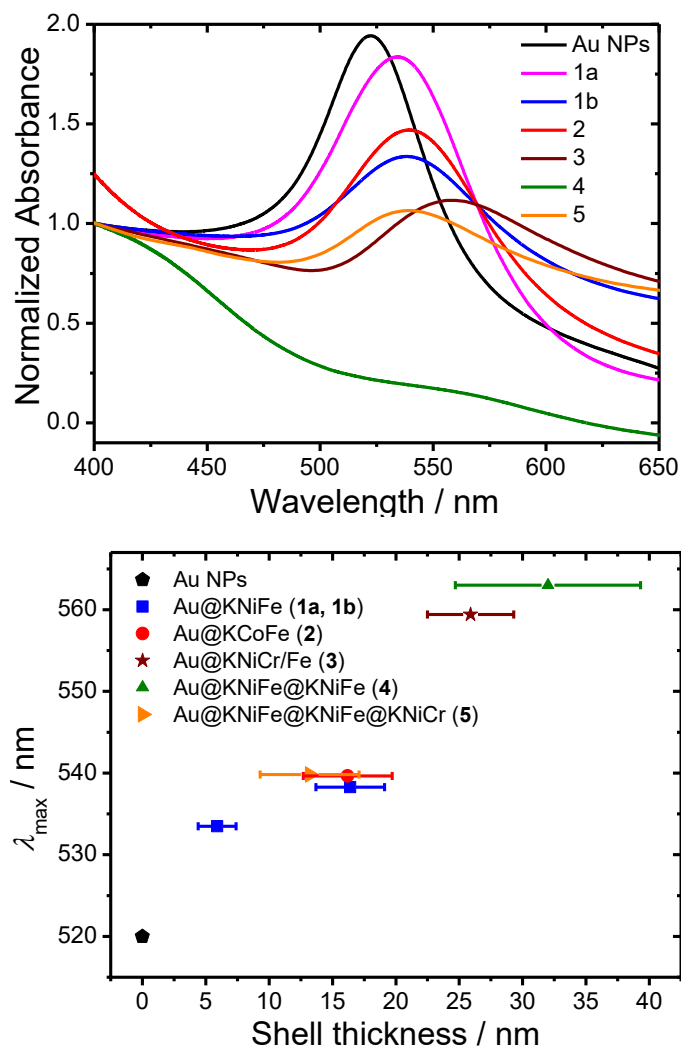
Fig. 3. a) UV-Vis spectra in aqueous suspension for **1-5** normalized at 400 nm. b) Dependence of the SPR maximum as a function of the shell thickness.

Magnetic Properties

The magnetic properties of the nanoheterostructures were studied using a SQUID-MPMS magnetometer working in the temperature range 1.8 – 350 K up to 7 T by using static (direct current (dc)) and dynamic (alternate current (ac)) modes. The magnetic measurements have been performed on samples diluted in PVP matrices (PVP, 1 wt % of nanoparticles). Such dilution method has been used previously in the case of PBA nanoparticles.[20, 58-60]

Magnetic properties of *Au@K/Ni/[Cr^{III}(CN)$_6$]:[Fe^{II}(CN)$_6$]* system 3

In our previous publications, we reported the magnetic properties for Au core@K/Ni/[Fe^{II}(CN)$_6$]@K/Ni/[Cr^{III}(CN)$_6$] shells nanoheterostructures having magnetic K/Ni/[Cr^{III}(CN)$_6$] shells of different size ranging from 1.6 to 40.5 nm. It has been shown that in the case of small magnetic shells (smaller than 7 nm), surface and interface spin frustrations induce an appearance of a spin glass like regime, while for the larger shells a long-range magnetic ordering is operational.

Here, we investigate the magnetic behaviour of Au@K/Ni/[Cr^{III}(CN)$_6$]:[Fe^{II}(CN)$_6$] core@shell nanoheterostructures **3**, with the solid solution shell (where [Cr^{III}(CN)$_6$]:[Fe^{II}(CN)$_6$)] ratio of 0.4). The ZFC-FC magnetization curves for **3** are shown in Fig. 4. Following the usual procedure, the ZFC curve was obtained with the sample being first cooled down with a zero magnetic field to 1.8 K, before being heated up under an applied magnetic field of 100 Oe in order to observe the "un-freezing" temperature (*i.e.* the temperature corresponding to the alignment of the magnetic moments initially frozen randomly). The FC curve is obtained by monitoring the change of the magnetization with temperature as the sample is cooled down with its magnetic moments aligned with a constant magnetic field of 100 Oe. The ZFC curve shows a maximum temperature at 14 K, while the FC curve exhibits an inflexion point at around 30 K and then continuously increases, indicating the presence of a magnetic irreversibility. This is further confirmed by the field dependence of the magnetization at 2.5 K, which shows the opening of the hysteresis loop with a coercive field of 146 Oe.
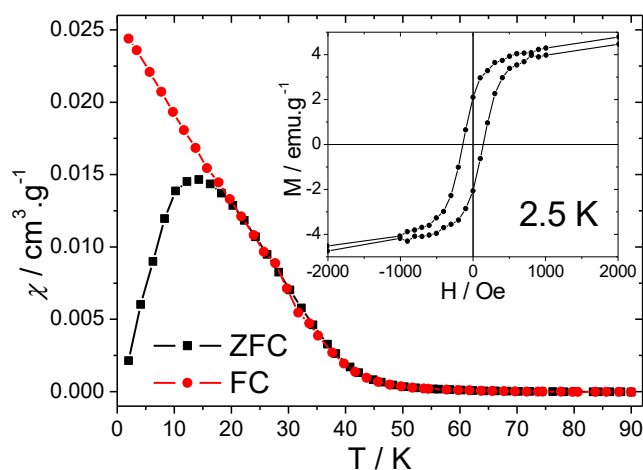

Fig. 4. ZFC/FC magnetization curves performed for **3** diluted in PVP with an applied magnetic field of 100 Oe. Inset: hysteresis loop at 2.5 K.

The dynamics of the magnetization were further studied by ac measurements. Both, χ' and χ'' show a frequency dependent behaviour indicating a slow relaxation of the magnetization (Fig. 5). Such features may originate from: (*i*) superparamagnetic regime of non-interacting or weakly interacting nanoparticles,[61] or (*ii*) intraparticle spin glass-like regime.[62] Calculating the Mydosh parameter, defined as $\varphi = (T_{max} - T_{min})/(T_{max} \times \log \nu_{max} - \log \nu_{min})$, which indicates the amplitude of the out-of-phase maxima's shift with frequency, could be first used to discriminate between these behaviours. This parameter is found equal to 0.062, which is largely below the superparamagnetic limit ($\varphi > 0.1$). The dynamic behaviour of the conventional superparamagnets can be described by a Néel model with an Arrhenius law, $\tau = \tau_0 \exp(E_a/kT)$, (where E_a is the average energy barrier for the reversal of the magnetization, τ_0 is the attempt time and k_B is the Boltzmann constant), obtained by plotting the temperature dependence of the relaxation time (extracted from the maximum of χ''). The obtained parameters for **3** gave: E_a = 630 K and τ_0 = 3.7 × 10^{-18} s (Fig. S15, Table 2). The value of τ_0 is clearly too low in

comparison with the ones expected for superparamagnetic systems (10^{-8} - 10^{-12} s) and has no physical meaning.
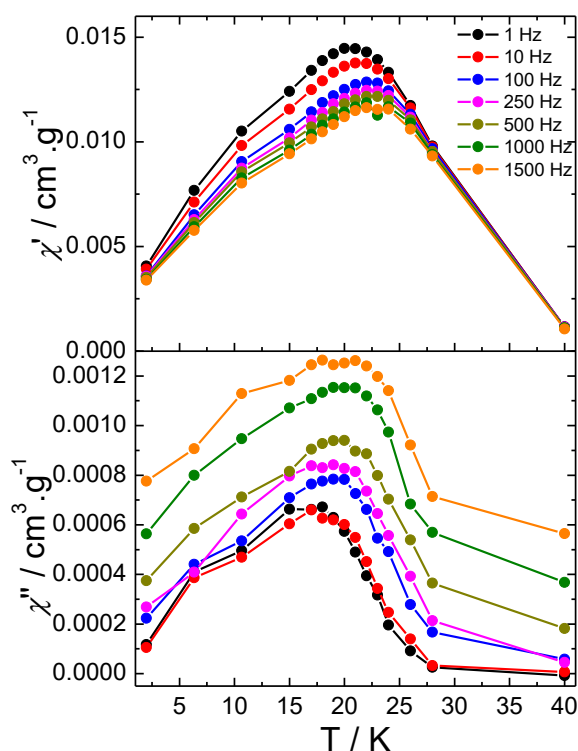

Fig. 5. Temperature dependence of the in-phase, χ', (top) and out-of-phase susceptibility, χ'', (bottom) for diluted sample **3**.

Fitting of the relaxation time with the critical scaling law for spin-glasses, $\tau = \tau_0[T_g/(T_{max} - T_g)]^{zv}$, where T_g is the glass temperature and zv is the critical exponent, corroborates the occurrence of a spin-glass regime with the following parameters: $\tau_0 = 2.0 \times 10^{-7}$ s; T_g = 14.1 K; zv = 7.6 (Table 2). The zv critical exponent is in the range of values expected for conventional spin glasses (4 < zv < 12),[62] while T_g remarkably agrees with the maximum of the ZFC curve. These parameters may be compared with the previously reported magnetic data for core@shell Au@K/Ni/[Fe^{II}(CN)$_6$]@K/Ni/[Cr^{III}(CN)$_6$] having a comparable ferromagnetic shell thickness of K/Ni/[Cr^{III}(CN)$_6$] of 10.5 nm, which exhibits T_{max} = 46.6 K and H_c = 169 Oe (Table 2) without a slow relaxation of the magnetization.[44] Clearly, the presence of the diamagnetic [Fe^{II}(CN)$_6$]$^{4-}$ moieties in the mixed shell makes the exchange interactions between the Cr^{3+}-CN-Ni^{2+} pairs much weaker, that induces the appearance of the spin-glass behaviour. This fact is in perfect agreement with the previously mentioned results of STEM-HAADF confirming the homogeneous distribution of Fe(II) and Cr(III) within the shell and the formation of a solid solution.

In order to further confirm this scenario, magnetic measurements on the model bulk

K$_{0.51}$Ni[Cr^{III}(CN)$_6$]$_{0.22}$[Fe^{II}(CN)$_6$]$_{0.51}$ compound with the similar [Cr^{III}(CN)$_6$]$^{3-}$/[Fe^{II}(CN)$_6$]$^{4-}$ ratio. Since the sample is composed by aggregated nanoparticles (*i.e.* 200-300 nm), dilution in the PVP matrix was performed similarly than for the other samples. The ZFC/FC curves show very closed shapes with T_{max} = 4.5 K (Fig. S16) and the field dependence of the magnetization exhibits the hysteretic behaviour with a smaller coercive field of 40 Oe (Insert Fig. S16). The dynamic of the relaxation monitored by ac measurements for the bulk solid solution (Fig. S17) also confirms the slow relaxation of the magnetization in accordance with a spin-glass regime. These results suggest that sample **3** exhibits a classical spin-glass behaviour arises from the disorder and spin frustration characteristic for the mixed PBA.
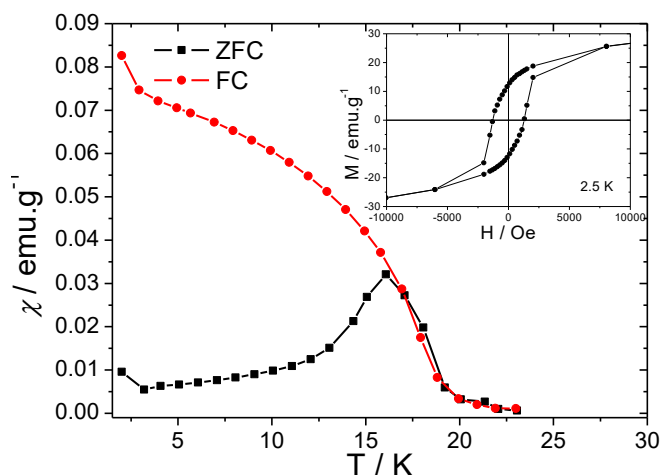
Magnetic properties of Au@K/Ni/[Fe^{II}(CN)$_6$]@K/Ni/[Fe^{III}(CN)$_6$] 4.

In our previously reported core@shell@shell systems Au@K/Ni/[Fe^{II}(CN)$_6$]@K/Ni/[Cr^{III}(CN)$_6$],[43-44] the observed coercive fields have been found relatively moderate (less than 200 Oe) in comparison to other PBA, such as for instance the bulk Ni$_3$[Fe^{III}(CN)$_6$]$_2$. This latter presents a ferromagnetic ordering temperature below 24 K in the dehydrated form,[63] while it is of 18.9 K when crystallized water molecules are present.[64] Thus, we have chosen to investigate the magnetic properties of Au@K/Ni/[Fe^{II}(CN)$_6$]@K/Ni/[Fe^{III}(CN)$_6$] **4** heterostructures having the K/Ni/[Fe^{III}(CN)$_6$] ferromagnetic shell of 14 nm to confirm the increase of the overall anisotropy arising from the presence of Fe^{III}. The ZFC curve shows a maximum temperature at 17 K and an increase below 4 K, while the FC curves continuously increases and exhibits inflection points at 18 K and 4 K (Fig. 6). The coercive field measured at 2.5 K is equal to 1300 Oe, which is comparable to the one found for the hydrated bulk analogous.[63] Due to the large shell thickness of K/Ni/[Fe^{III}(CN)$_6$] ferromagnetic shell (14 nm), the overall behaviour appears comparable to the bulk form, except the increase observed on the ZFC/FC curves at low temperature. This latter can be imputed to the presence of the first paramagnetic K/Ni/[Fe^{II}(CN)$_6$] shell, which shows magnetic interaction between the Ni^{2+} ions through the diamagnetic [Fe^{II}(CN)$_6$]$^{4-}$ bridge.[44]

Such scenario is ultimately confirmed by measuring the dynamic of the relaxation of the magnetization in the ac mode, which shows a frequency independent behaviour (Fig. S18) characteristic of a long-range magnetic ordering.

Table 2: Magnetic parameters for the core@shell nanoheterostructures **1-5**.

Sample	T_{max} (K)	H_c (Oe)	Mydosh parameter φ	Arrhenius law		Scaling law		
				E_a/k_B, (K)	τ_0, (s)	T_g, (K)	τ_0, (s)	zv
3	14	146	0.062	630	3.7×10^{-18}	14.1	2.0×10^{-7}	7.6
4	17	1300	-	-	-	-	-	-
5	35	200	0.027	3651	6.0×10^{-18}	21.3	0.56	33.8

Fig. 6. ZFC/FC magnetization curves performed for **4** with an applied magnetic field of 100 Oe. Inset: hysteresis loop for **4** at 2.5 K.

Magnetic properties of Au@K/Ni/[Fe^{II}(CN)$_6$]@K/Ni/[Fe^{III}(CN)$_6$]@K/Ni/[Cr^{III}(CN)$_6$] 5.

The core@shell@shell@shell systems Au@K/Ni/[Fe^{II}(CN)$_6$]@K/Ni/[Fe^{III}(CN)$_6$]@K/Ni/[Cr^{III}(CN)$_6$] **5** for which the second and third PBA shells are both ferromagnetic were designed to study hard-soft magnetic heterostructures. The bulk Ni$_3$[Cr^{III}(CN)$_6$]$_2$ PBA presents a ferromagnetic ordering temperature, which varies from 53 K up to 90 K for CsNi[Cr^{III}(CN)$_6$] depending on the amount of cyanometallate vacancies.[3] In contrast to **4**, the shell thicknesses of both ferromagnetic PBA shells are relatively thin (5 and 3 nm, respectively for the second and third shells). This should lead to a different magnetic behaviour with respect to the usual large shells exhibiting bulk-like ferromagnetic ordering. The ZFC curve shows a large peak with a maximum at 35 K, while the FC curve exhibits an inflection point around 60 K, close to the Curie temperature of the bulk Ni$_3$[Cr^{III}(CN)$_6$]$_2$ compound. The field dependence of the magnetization measured at 2.5 K shows the presence of a smooth hysteresis loop with a coercive field value, H_c, of 200 Oe. Noticeably, the latter is greater than the value found for the bulk Ni$_3$[Cr(CN)$_6$]$_2$ analogue (120 Oe).[65] The absence of kinks in the curve indicates that both PBA magnetic phases are intimately coupled.

In usual magnetic hard core@soft shell nanoparticles, the hysteresis loop depends strongly on the thickness of the soft shell.[66-67] Since the shell molar fraction is a non-linear function of the shell thickness, minor variation in the shell thickness leads to dramatic changes in the volume fraction. Thus, for shell thickness roughly twice larger than the domain wall size of the hard phase, δ_{W-H}, the magnetization reversal is dominated by the large soft shell implying a decrease of the observed coercive field. In the case of **5**, the K/Ni/[Cr^{III}(CN)$_6$] volume fraction $f = V_{shell}/V_{total}$ (taken into account all shells) is close to 0.5, assuming regular PBA cubes as shells. This clearly confirms the larger amount of the soft K/Ni/[Cr^{III}(CN)$_6$] with respect to the hard K/Ni/[Fe^{III}(CN)$_6$] one. Thus, the low value of H_c = 200 Oe is consistent with a behaviour dominated by the external K/Ni/[Cr^{III}(CN)$_6$] shell.
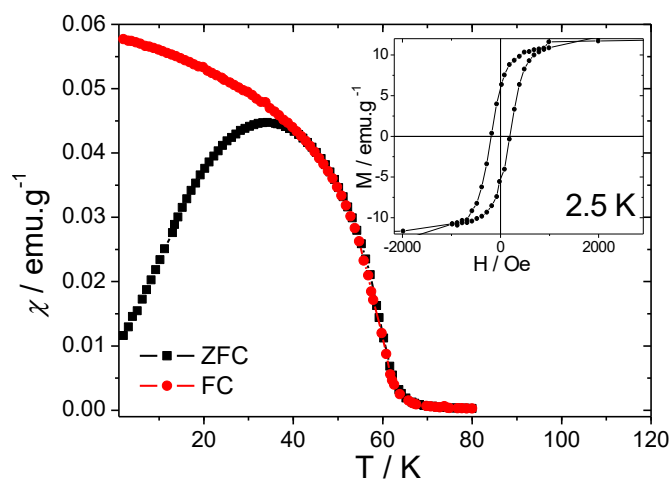
Fig. 7. ZFC/FC magnetization curves performed for **5** diluted in PVP with an applied magnetic field of 100 Oe. Inset: hysteresis loop at 2.5 K.

The dynamic behaviour of compound **5** was investigated using alternate frequency (ac) measurements. The temperature dependences of the in-phase (χ') and out-of-phase (χ'') susceptibilities were measured in a zero dc-field with frequencies ranging from 1 Hz to 1488 Hz. Fig. 8 shows a clear frequency dependence of both, χ' and χ'' components. At 1 Hz frequency, χ' and χ'' exhibits peaks at 49.0 K and 43.4 K, respectively. It can be noted that the amplitude of χ'' increases with frequency, which is often characteristic for systems presenting a spin-glass behaviour. This is further confirmed by calculating the Mydosh, which is found equal to 0.027, largely below the superparamagnetic limit ($\varphi > 0.1$) and by the fitting of the temperature dependence of the relaxation time with an Arrhenius law, giving E_a = 3651 K and $\tau_0 = 6.0 \times 10^{-18}$ s (Fig. S19, Table 2).
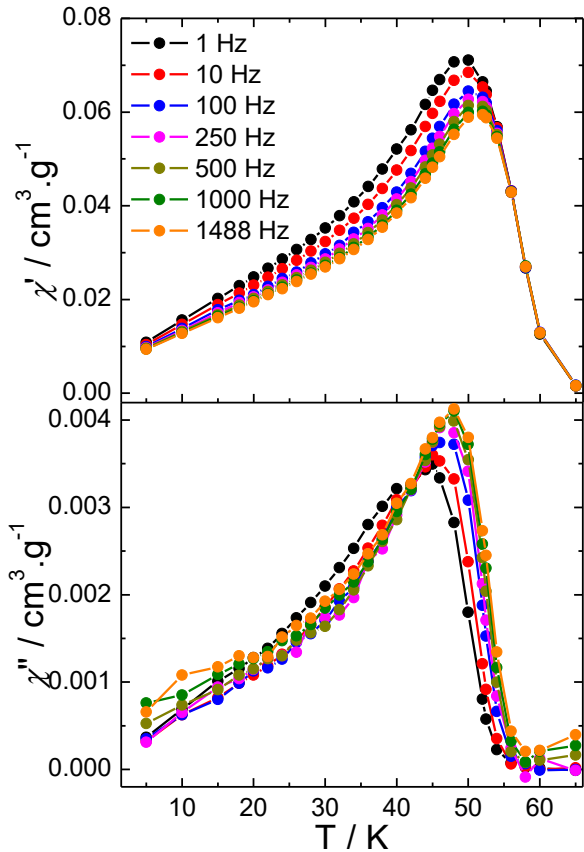
Fig. 8. Temperature dependence of the in-phase, χ', (top) and out-of-phase susceptibility, χ'', (bottom) with a zero dc magnetic field for diluted sample **4**.

Due to the high dilution rates used in our case (1 wt % of nanoparticles), the presence of strong magnetostatic interactions can be ruled out. Consequently, the observed behaviour may reflect an intrinsic spin-glass regime. To further check this, the thermal variation of the relaxation time was fitted using the critical scaling law of spin glasses ($\tau = \tau_0[T_g/(T_{max} - T_g)]^{zv}$, see above for details) , giving the parameters: $\tau_0 = 0.56$ s; $T_g = 21.3$ K and $zv = 33.8$, which are out of the limits defined for traditional spin-glasses (4 < zv < 12).[62] This fact can be ascribed to the complex behaviour induced by the presence of both, interface and surface spin frustrations, which cannot be simply described by classical spin-glass model. Such behaviour has previously been observed for other Au@ K/Ni/[Fe^{II}(CN)$_6$]@K/Ni/[Cr^{III}(CN)$_6$] systems with a similar K/Ni/[Fe^{III}(CN)$_6$] thickness.[44]

Lastly, the occurrence of a spin glass-like regime is ultimately confirmed by monitoring the dc field dependence of the ac susceptibility with an oscillating field frequency of 100 Hz (Fig. 9). Applying dc magnetic fields induces a shift to lower temperatures of the χ' and χ'' maxima. Fields larger than 400 Oe induce the complete disappearance of out-of-phase signals. The temperature dependence of the χ'' maximum follows the Almeida-Thouless (AT) equation, $H \propto (1 - T_{max}/T_f)^{3/2}$,[68] T_f being the freezing temperature. Such field dependence is usually considered as a spin-glass signature.[69] Extrapolation of the AT line at $H = 0$ Oe yields $T_f = 43.5$ K (Fig. S20). This value is slightly larger than the ZFC $T_{max} = 35$ K value (obtained under a 100 Oe DC field).

Thus, the magnetic data indicate that the Au@K/Ni/[Fe^{II}(CN)$_6$]@K/Ni/[Fe^{III}(CN)$_6$]@K/Ni/[Cr^{III}(CN)$_6$] heterostructures exhibit a complex spin-glass behaviour, which is in agreement to what we already reported for the Au@K/Ni/[Fe^{II}(CN)$_6$@K/Ni/[Cr^{III}(CN)$_6$] nanoparticles with double shell.[44] Clearly, the dc overall magnetic behaviour appears to be dominated by the third external K/Ni/[Cr^{III}(CN)$_6$] shell, which exhibits the highest volume fraction. However, the small thickness (below the domain size) associated with the presence of interface and/or surface spin-frustration induces a complex spin-glass behaviour.
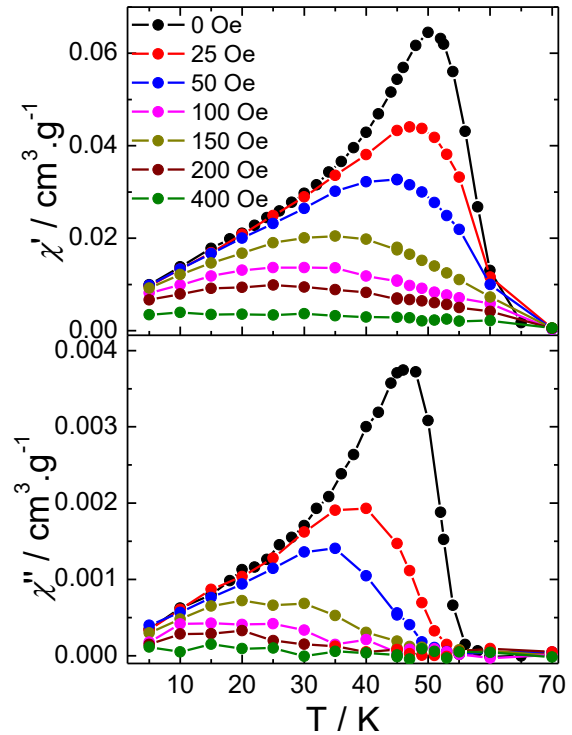

Fig. 9. Temperature dependence of the in-phase, χ', (top) and out-of-phase susceptibility, χ'', (bottom) with various dc fields for diluted sample **5**.

Conclusions

Au core@PBA shell heterostructures can be viewed as elegant and versatile multifunctional systems combining the plasmonic property of the gold nanoparticles with the magnetic behaviour of PBA. Remarkably designing multishell systems allow tuning both of these properties. In this study, we synthesize a series of new Au core@PBA shell systems with one, two and three different PBA shells and investigate their optical and magnetic properties.

First, we have investigated the Au/PBA interface in the Au@K/Ni/[Fe^{II}(CN)$_6$] system with different shell thicknesses and demonstrated by the XPS technique the presence of the Au^{I}/CN$^-$ and/or Au^{III}/CN$^-$ species located at the surface of the gold nanoparticles. These species stabilize the gold nanoparticles in solution and can be used as anchoring points to growth PBA shells through coordination with divalent metal ions. This explains (among others) the differences in reactivity depending on the targeted PBA analogues.

Thus, taking into account this fact, we have shown for the first time that it is possible to extend our synthetic strategy to other PBA shells through design of $Au@K/Co/[Fe^{II}(CN)_6]$ heterostructures. These new nano-objects present well determined shape with the Au core surrounded by the distinct cubic PBA shell. Their electronic spectra exhibit the SPR band, which is red shifted in comparison with the pristine Au nanoparticles due to the presence of the PBA shell. The optical properties are in agreement with the ones previously reported for other Au core@PBA shell nanoparticles.

Thirdly, we have demonstrated that $Au@K/Ni/[Fe^{II}(CN)_6]:[Cr^{III}(CN)_6]$ nano-object with a solid solution of two PBA in the shell may be designed. Remarkably, they present the magnetic shell in direct contact with the plasmonic gold. These nano-objects present both, the optical properties (SPR band) and the spin glass-like magnetic behaviour. The latter is in good agreement with the expected behaviour for spin diluted systems, such as magnetic solid solutions.

Fourth, we have demonstrated that $Au@K/Ni/[Fe^{II}(CN)_6]$ heterostructures can be used as a versatile platform to design Au core@PBA multishell systems, which allow an accurate tuning of both, optical and magnetic properties. Thus, the design of $Au@K/Ni/[Fe^{II}(CN)_6]@K/Ni/[Fe^{III}(CN)_6]$ heterostructures with double PBA shell permits to take advantage of the magnetic anisotropy of the $K/Ni/[Fe^{III}(CN)_6]$ analogue to obtain a substantial magnetic coercivity. The subsequent growing of different PBA allows the design of triple-shell $Au@K/Ni/[Fe^{II}(CN)_6]@K/Ni/[Fe^{III}(CN)_6]@$ $Au@K/Ni/[Fe^{II}(CN)_6]@K/Ni/[Cr^{III}(CN)_6]$ exchange-coupled heterostructures. The resulting magnetic characteristics are governed by the external $K/Ni/[Cr^{III}(CN)_6]$ shell presenting the highest volume fraction. They exhibit a complex dynamic behaviour resulting from a spin frustration confirming that such heterostructures exhibit a great versatility and constitute the first step towards the investigation of the synergy between magnetic and plasmonic properties.

Acknowledgements

There are no conflicts of interest to declare.

Notes and references

‡ Footnotes relating to the main text should appear here. These might include comments relevant to but not central to the matter under discussion, limited experimental and spectral data, and crystallographic data.

1   S. Kitagawa, R. Kitaura and S.-i. Noro, *Angew. Chem. Int. Edit.*, 2004, **43**, 2334-2375.
2   H. Tokoro and S.-i. Ohkoshi, *Dalton Trans.*, 2011, **40**, 6825-6833.
3   M. Verdaguer and G. S. Girolami, in *Magnetism: Molecules to Materials V*, Wiley-VCH Verlag GmbH & Co. KGaA, 2005, DOI: 10.1002/3527604383.ch9, pp. 283-346.
4   J. Duan, W. Jin and S. Kitagawa, *Coord. Chem. Rev.*, 2017, **332**, 48-74.
5   D. DeSantis, J. A. Mason, B. D. James, C. Houchins, J. R. Long and M. Veenstra, *Energy & Fuels*, 2017, **31**, 2024-2032.
6   L. Ouahab, *Multifunctional molecular materials*, Pan Stanford, Singapore, 2013.
7   X. Song, T. K. Kim, H. Kim, D. Kim, S. Jeong, H. R. Moon and M. S. Lah, *Chem. Mater.*, 2012, **24**, 3065-3073.
8   W. R. Lee, D. W. Ryu, W. J. Phang, J. H. Park and C. S. Hong, *Chem. Commun.*, 2012, **48**, 10847-10849.
9   T. Fukushima, S. Horike, H. Kobayashi, M. Tsujimoto, S. Isoda, M. L. Foo, Y. Kubota, M. Takata and S. Kitagawa, *J. Am. Chem. Soc.*, 2012, **134**, 13341-13347.
10 C. G. Carson, J. Ward, X. T. Liu, J. Schwartz, R. A. Gerhardt and R. Tannenbaum, *J. Phys. Chem. C*, 2012, **116**, 15322-15328.
11 S. Furukawa, K. Hirai, K. Nakagawa, Y. Takashima, R. Matsuda, T. Tsuruoka, M. Kondo, R. Haruki, D. Tanaka, H. Sakamoto, S. Shimomura, O. Sakata and S. Kitagawa, *Angew. Chem. Int. Edit.*, 2009, **48**, 1766-1770.
12 B. Liu, M. Tu, D. Zacher and R. A. Fischer, *Adv. Funct. Mater.*, 2013, **23**, 3790-3798.
13 S. Furukawa, K. Hirai, Y. Takashima, K. Nakagawa, M. Kondo, T. Tsuruoka, O. Sakata and S. Kitagawa, *Chem. Commun.*, 2009, DOI: 10.1039/B909993J, 5097-5099.
14 N. L. Torad, M. Hu, M. Imura, M. Naito and Y. Yamauchi, *J. Mater. Chem.*, 2012, **22**, 18261-18267.
15 M. Hu, S. Furukawa, R. Ohtani, H. Sukegawa, Y. Nemoto, J. Reboul, S. Kitagawa and Y. Yamauchi, *Angew. Chem., Int. Ed.*, 2012, **51**, 984-988, S984/981-S984/910.
16 M. Hu, A. A. Belik, M. Imura and Y. Yamauchi, *J. Am. Chem. Soc.*, 2013, **135**, 384-391.
17 O. N. Risset, E. S. Knowles, S. Ma, M. W. Meisel and D. R. Talham, *Chem. Mater.*, 2013, **25**, 42-47.
18 W. Zhang, Y. Zhao, V. Malgras, Q. Ji, D. Jiang, R. Qi, K. Ariga, Y. Yamauchi, J. Liu, J.-S. Jiang and M. Hu, *Angew. Chem. Int. Edit.*, 2016, **55**, 8228-8234.
19 L. Catala, D. Brinzei, Y. Prado, A. Gloter, O. Stéphan, G. Rogez and T. Mallah, *Angew. Chem. Int. Edit.*, 2009, **48**, 183-187.
20 Y. Prado, N. Dia, L. Lisnard, G. Rogez, F. Brisset, L. Catala and T. Mallah, *Chem. Commun.*, 2012, **48**, 11455-11457.
21 M. F. Dumont, E. S. Knowles, A. Guiet, D. M. Pajerowski, A. Gomez, S. W. Kycia, M. W. Meisel and D. R. Talham, *Inorg. Chem.*, 2011, **50**, 4295-4300.
22 N. Dia, L. Lisnard, Y. Prado, A. Gloter, O. Stéphan, F. Brisset, H. Hafez, Z. Saad, C. Mathonière, L. Catala and T. Mallah, *Inorg. Chem.*, 2013, **52**, 10264-10274.
23 O. N. Risset, P. A. Quintero, T. V. Brinzari, M. J. Andrus, M. W. Lufaso, M. W. Meisel and D. R. Talham, *J. Am. Chem. Soc.*, 2014, **136**, 15660-15669.
24 M. Presle, J. Lemainque, J. M. Guigner, E. Larquet, I. Maurin, J. P. Boilot and T. Gacoin, *New. J. Chem.*, 2011, **35**, 1296-1301.
25 M. Presle, I. Maurin, F. Maroun, R. Cortès, L. Lu, R. Sayed Hassan, E. Larquet, J.-M. Guigner, E. Rivière, J. P. Wright, J.-P. Boilot and T. Gacoin, *J. Phys. Chem. C*, 2014, **118**, 13186-13195.
26 D. Asakura, C. H. Li, Y. Mizuno, M. Okubo, H. Zhou and D. R. Talham, *J. Am. Chem. Soc.*, 2013, **135**, 2793-2799.
27 M. Okubo, C. H. Li and D. R. Talham, *Chem. Commun.*, 2014, **50**, 1353-1355.
28 C. R. Gros, M. K. Peprah, B. D. Hosterman, T. V. Brinzari, P. A. Quintero, M. Sendova, M. W. Meisel and D. R. Talham, *J. Am. Chem. Soc.*, 2014, **136**, 9846-9849.

29 C. R. Gros, M. K. Peprah, A. C. Felts, T. V. Brinzari, O. N. Risset, J. M. Cain, C. F. Ferreira, M. W. Meisel and D. R. Talham, *Dalton Trans.*, 2016, **45**, 16624-16634.

30 G. Lu, S. Li, Z. Guo, O. K. Farha, B. G. Hauser, X. Qi, Y. Wang, X. Wang, S. Han, X. Liu, J. S. DuChene, H. Zhang, Q. Zhang, X. Chen, J. Ma, S. C. J. Loo, W. D. Wei, Y. Yang, J. T. Hupp and F. Huo, *Nat Chem*, 2012, **4**, 310-316.

31 F. Ke, L.-G. Qiu, Y.-P. Yuan, X. Jiang and J.-F. Zhu, *J. Mater. Chem.*, 2012, **22**, 9497-9500.

32 P. L. Feng, J. J. Perry Iv, S. Nikodemski, B. W. Jacobs, S. T. Meek and M. D. Allendorf, *J. Am. Chem. Soc.*, 2010, **132**, 15487-15489.

33 Y. Li, J. Tang, L. He, Y. Liu, Y. Liu, C. Chen and Z. Tang, *Adv. Mater.*, 2015, **27**, 4075-4080.

34 a) L. He, Y. Liu, J. Liu, Y. Xiong, J. Zheng, Y. Liu and Z. Tang, *Angewandte Chemie*, 2013, **125**, 3829-3833; b) T. Ishida, M. Nagaoka, T. Akita, M. Haruta, *Chem. Eur. J.* **2008**, **14**, 8456-8460.

35 F. Ke, J. Zhu, L.-G. Qiu and X. Jiang, *Chem. Commun.*, 2013, **49**, 1267-1269.

36 S. S. Kumar, J. Joseph and K. L. Phani, *Chem. Mater.*, 2007, **19**, 4722-4730.

37 J.-D. Qiu, H.-Z. Peng, R.-P. Liang, J. Li and X.-H. Xia, *Langmuir*, 2007, **23**, 2133-2137.

38 Z. Song, R. Yuan, Y. Chai, B. Yin, P. Fu and J. Wang, *Electrochimica Acta*, 2010, **55**, 1778-1784.

39 P. Ni, Y. Zhang, Y. Sun, Y. Shi, H. Dai, J. Hu and Z. Li, *RSC Adv.*, 2013, **3**, 15987-15992.

40 A. V. Narendra Kumar and J. Joseph, *RSC Adv.*, 2014, **4**, 10975-10981.

41 L. Jing, X. Liang, Z. Deng, S. Feng, X. Li, M. Huang, C. Li and Z. Dai, *Biomaterials*, 2014, **35**, 5814-5821.

42 P. C. Pandey, R. Singh and Y. Pandey, *RSC Adv.*, 2015, **5**, 49671-49679.

43 G. Maurin-Pasturel, J. Long, Y. Guari, F. Godiard, M.-G. Willinger, C. Guerin and J. Larionova, *Angew. Chem., Int. Ed.*, 2014, **53**, 3872-3876.

44 G. Maurin-Pasturel, J. Long, M. A. Palacios, C. Guerin, C. Charnay, M. G. Willinger, A. A. Trifonov, J. Larionova and Y. Guari, *Chem. Eur. J.*, 2017, **23**, 7483-7496.

45 C.-C. Huang, W.-C. Lai, C.-Y. Tsai, C.-H. Yang and C.-S. Yeh, *Chem. Eur. J.*, 2012, **18**, 4107-4114.

46 A. McNeillie, D. H. Brown, W. E. Smith, M. Gibson and L. Watson, *J. Chem. Soc., Dalton Trans.*, 1980, DOI: 10.1039/DT9800000767, 767-770.

47 P. D. Fawell, C. F. Vernon, C. Klauber and H. G. Linge, *Reactive Polymers*, 1992, **18**, 57-65.

48 A. Senthil Kumar, P. Barathi and K. Chandrasekara Pillai, *J. Electroanal. Chem.*, 2011, **654**, 85-95.

49 A. Bleuzen, C. Lomenech, V. Escax, F. Villain, F. Varret, C. Cartier dit Moulin and M. Verdaguer, *J. Am. Chem. Soc.*, 2000, **122**, 6648-6652.

50 O. N. Risset and D. R. Talham, *Chem. Mater.*, 2015, **27**, 3838-3843.

51 P. E. Chow, *Gold Nanoparticles: Properties, Characterization and Fabrication*, Nova Science Publishers, 2010.

52 N. Li, P. Zhao and D. Astruc, *Angew. Chem. Int. Edit.*, 2014, **53**, 1756-1789.

53 H. Chen, L. Shao, Q. Li and J. Wang, *Chem. Soc. Rev.*, 2013, **42**, 2679-2724.

54 N. S. Pesika, K. J. Stebe and P. C. Searson, *J. Phys. Chem. B*, 2003, **107**, 10412.

55 M. A. Garcia, *J. Phys. D: Appl. Phys.*, 2011, **44**, 283001.

56 K. M. Mayer and J. H. Hafner, *Chem. Rev.*, 2011, **111**, 3828-3857.

57 R. T. Tom, A. S. Nair, N. Singh, M. Aslam, C. L. Nagendra, R. Philip, K. Vijayamohanan and T. Pradeep, *Langmuir*, 2003, **19**, 3439-3445.

58 D. Brinzei, L. Catala, N. Louvain, G. Rogez, O. Stephan, A. Gloter and T. Mallah, *J. Mater. Chem.*, 2006, **16**, 2593-2599.

59 Y. Prado, L. Lisnard, D. Heurtaux, G. Rogez, A. Gloter, O. Stephan, N. Dia, E. Riviere, L. Catala and T. Mallah, *Chem. Commun.*, 2011, **47**, 1051-1053.

60 Y. Prado, S. Mazerat, E. Rivière, G. Rogez, A. Gloter, O. Stéphan, L. Catala and T. Mallah, *Adv. Funct. Mater.*, 2014, **24**, 5402-5411.

61 L. Néel, *Adv. Phys.*, 1955, **4**, 191.

62 J. A. Mydosh, *Spin glasses : an experimental introduction*, Taylor & Francis, London; Washington, DC, 1993.

63 S. Juszczyk, C. Johansson, M. Hanson, A. Ratuszna and G. Malecki, *J. Phys.: Condens. Matter*, 1994, **6**, 5697.

64 R. Martinez-Garcia, M. Knobel and E. Reguera, *J. Phys.: Condens. Matter*, 2006, **18**, 11243.

65 S.-i. Ohkoshi, T. Iyoda, A. Fujishima and K. Hashimoto, *Phys. Rev. B*, 1997, **56**, 11642-11652.

66 A. López-Ortega, M. Estrader, G. Salazar-Alvarez, A. G. Roca and J. Nogués, *Physics Reports*, 2015, **553**, 1-32.

67 S. H. Moon, S.-h. Noh, J.-H. Lee, T.-H. Shin, Y. Lim and J. Cheon, *Nano Lett.*, 2017, **17**, 800-804.

68 J. R. L. d. Almeida and D. J. Thouless, *J. Phys. A: Math. Gen.*, 1978, **11**, 983.

69 L. Lartigue, S. Oh, E. Prouzet, Y. Guari and J. Larionova, *Materials Chemistry and Physics*, 2012, **132**, 438-445.